INVESTIGATING THE EFFECT OF DELAMINATION-INDUCED FRICTIONAL CONTACT ON THE DYNAMIC BEHAVIOR OF LAMINATE STRUCTURES

INVESTIGATING THE EFFECT OF DELAMINATION-INDUCED FRICTIONAL CONTACT ON THE DYNAMIC BEHAVIOR OF LAMINATE STRUCTURES

Sh. Kiasat[1], A. S. Nobari[2], M. Filippi[1] & E. Carrera[1]

[1]Mul2 Group, Department of Mechanical and Aerospace Engineering, Politecnico di Torino, 10129 Torino, Italy
[2]Aeronautics Engineering Department, Imperial College, Exhibition Road, London SW7 2AZ, United Kingdom

Abstract

The presence of interlaminar delamination in laminate structures has a significant impact on their structural behavior, stiffness, and operational life. Understanding the role of frictional contact between delaminated interfaces is essential for dissipating energy and reducing vibrations, thereby affecting structural dynamics. This research thoroughly investigates the friction-damping mechanism using time and frequency domain analyses. It explores the possibility of using energy indicators such as strain or frictional dissipated energy and modal parameters like natural damped frequency reliable damage indices to detect and evaluate delamination in laminated structures. Moreover, the paper examines the contribution of frictional contact damping to the overall dynamic behavior. Moreover, through numerical simulations, the aim is to enhance damage detection techniques, design strategies, and approaches to improve the performance and service life of laminates. The paper also presents different approaches and formulations to simulate contact mechanisms into finite element models. The findings and implications of this study have direct applications in guiding further research and facilitating the health monitoring of laminated structures.

Keywords: SHM, Delamination, Frictional contact, Damping, Damage detection

1. Introduction

Laminate structures are widely used in aerospace [1, 2, 3], automotive [4], and wind energy industries [5] due to their lightweight and robust properties. However, inter-laminar delamination poses a significant challenge to their reliability and safety. Detecting delamination is crucial to prevent potential catastrophic failure. Non-destructive testing (NDT) techniques, such as ultrasonic testing (UT) and thermography, are essential for detecting and assessing damages in laminate structures [6]. However, most current NDT methods require out-of-service, offline measurements and cannot be applied in real-time, except for oscillation-based techniques. Techniques like Ultrasound or Acoustic Emission necessitate offline measurements.

Conversely, oscillation-based methods, including Lamb waves and vibration-based techniques, enable real-time damage detection. Vibration-based Structural Health Monitoring (SHM) [7] techniques are advantageous due to their simplicity and cost-effectiveness [8]. Modal parameters, such as modal damping and natural frequencies, are sensitive indicators of delamination and can aid in targeted inspection and maintenance [9]. Inter-laminar delamination refers to the detachment of adjacent layers in laminated structures [10, 11], resulting in various harmful effects, such as reduced structural stiffness [12], shifts in resonance frequencies [13, 14], mode localization [15], variations in modal damping [16], and decreased fatigue life [17]. These effects weaken the structure and alter its behavior, affecting stiffness, vibration characteristics, and operational life. Frictional contact between delaminated interfaces plays a crucial role in dissipating energy and reducing vibrations. Understanding the mechanisms involved in energy dissipation and vibration reduction therefore is essential. Frictional contact generates forces that convert mechanical energy into heat, damping

structural vibrations. Parameters such as the inter-facial friction coefficient, contact area, and relative motion between the delaminated layers characterize the friction-damping mechanism in structures with inter-laminar delamination [18, 19, 20, 21]. Friction damping in delaminated structures exhibits several effects. Friction at delaminated interfaces affects the structure's damping ratio and dynamic response, thereby enhancing modal damping [22]. Friction damping effectively suppresses resonant vibrations, minimizing structural instability and fatigue.In their previous research, the researchers identified the modal damping parameter as a sensitive indicator of failures in laminated structures [9]. However, its extraction proved computationally expensive and challenging. This study investigates using energy indices alongside the damped natural frequency parameter to detect delamination in laminated structures.

This research also aims to analyze the contribution of frictional contact damping, arising from sliding and relative motion between delaminated layers to the overall dynamic behavior of delaminated structures. By quantifying the magnitude and influence of friction damping, particularly on parameters such as damped natural frequency strain energy, frictional dissipated energy and FRF characteristics, the study aims to enhance the understanding of delaminated structures' dynamic behavior and stability. To achieve these objectives, a comprehensive methodology integrating time and frequency-based methods is employed in this study. Dynamic explicit analysis is conducted on a finite element (FE) model of a laminated beam structure under dynamic sine-sweep loading, stimulating various natural modes across different frequencies. The model represents delamination by physically separating the FE nodes in the delaminated region. The penalty contact method [23, 24], known for its simplicity and computational efficiency, is used to simulate contact between these nodes. The classical Coulomb friction model [25] defines the tangential contact properties between the delaminated interfaces. The resulting time-history signals are analyzed using signal processing techniques, such as the Fast Fourier Transform (FFT), to obtain the laminated structure's Frequency Response Function (FRF). The findings of this research are expected to contribute to the development of improved damage detection techniques, design strategies, and approaches for enhancing the performance and durability of laminate structures. By gaining insights into the friction-damping mechanism and its impact on the overall dynamic response, this study aims to provide valuable knowledge for engineers and researchers working on non-destructive damage detection methods, especially in the context of delamination in laminated structures.

2. Computational Approach

2.1 FEM-Based Model Assumptions

The case study is a two-layer elastic beam with clamped-free boundary conditions (BCs) and subjected to a concentrated logarithmic sine-sweep load as depicted in Fig. 1. The material properties considered are Young's modulus (E) of 69 (GPa), density (ρ) of 2766 (kg/m^3), and Poisson's ratio (ν) of 0.3. The finite element mesh consisted of linear hexahedral elements. For the sake of brevity, the governing equations of the finite element model (FEM) are not provided in this context. Further details can be found in Ref. [27].

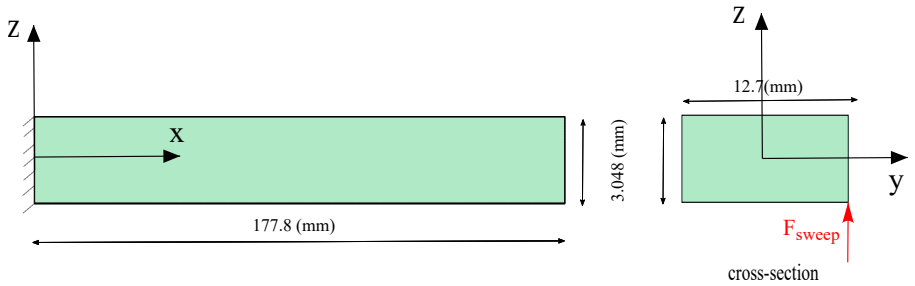

Fig. 1 – Schematic of the two-layered beam along with BCs and loading position

2.2 Modeling Frictional Contact

In this section, we examine the critical aspects of modeling contact behaviors within laminated structures, specifically focusing on normal and tangential contact behaviors. The normal contact aspect

primarily addresses the interaction between two debonded surfaces upon contact, while the tangential contact aspect encompasses the resistance to relative motions, often characterized by frictional effects.

2.2.1 Normal contact

In delaminated interfaces, normal contact refers to the interaction between separated layers or interfaces perpendicular to their contact area. Accurate modeling techniques are required to capture the normal contact behavior between the delaminated interfaces. Two commonly used approaches are the 'Micromechanical Approach', which considers material behavior at the contact area and develops constitutive laws for microscale response, and the 'Geometrical Constraint Approach', which focuses on contact geometry and ensures no overlap or penetration between bodies in the normal direction. The Geometrical Constraint Approach, often referred to as 'low contact precision', is a technique that emphasizes enforcing geometric constraints to capture essential contact behavior. It does so without explicitly modeling detailed material responses within the contact interface. The approach derives the determination of the normal contact pressure directly from the constraint equations without relying on a constitutive equation. Figure 2 provides a representation of the distance calculation, which is important in determining the gap or penetration between the two bodies. The parameterization of the boundary Γ^1 using convective coordinates is denoted by $\bar{\zeta} = (\bar{\zeta}^1, \bar{\zeta}^2)$. The relation between each point on the contact boundary of body 2 (Γ^2) and a corresponding point on the contact boundary of body 1 (Γ^1) can be established using the minimum distance problem (Eq. 1). This is done under the assumption that the contact boundary exhibits local convexity, a key factor in this calculation. Interested readers can refer to Refs. [28, 29, 30] for more detailed information.

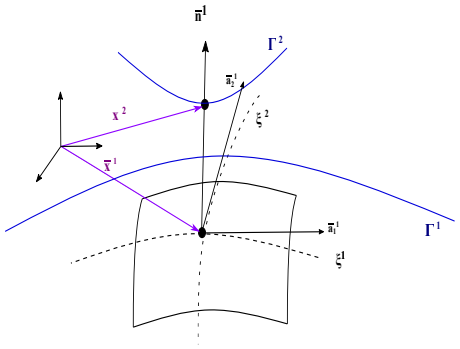

Fig. 2 – Coordinate system and minimum distance for normal contact of 3D bodies

$$\hat{d}^1\left(\xi^1,\xi^2\right) = \left\|x^2 - \bar{x}^1\right\| = \min_{x1\subseteq\Gamma 1} \left\|x^2 - \bar{x}^1\right\| \tag{1}$$

The point $\bar{x}^1$ is identified by meeting the necessary condition for minimizing the distance function in Eq. 1 as Eq. 2.

$$\frac{d}{d\xi^\alpha}\,\hat{d}^1\left(\xi^1,\xi^2\right) = \frac{x^2 - \bar{x}^1(\xi^1,\xi^2)}{\|x^2 - \bar{x}^1(\xi^1,\xi^2)\|}.\hat{x}^1_{,\alpha} = 0 \tag{2}$$

To solve Eq. 2, orthogonality between the first and second terms is required. The term represented by the tangent vector $\hat{x}^1_{,\alpha}(\xi^1,\xi^2)$, must align with the normal vector n^1 at the minimum point $(\bar{\xi}^1,\bar{\xi}^2)$. This results in the condition $-n^1\left(\bar{\xi}^1,\bar{\xi}^2\right).a^1_\alpha\left(\bar{\xi}^1,\bar{\xi}^2\right) = 0$, indicating that the current master point $\hat{x}^1(\bar{\xi}^1,\bar{\xi}^2)$ is the orthogonal projection of the given slave point x^2 onto the master surface $\varphi^1_t(\Gamma^1_c)$. The bar denotes evaluation at the minimal distance point. The non-penetration condition for contact is represented by Eq. 3.

$$g_N = (x_2 - \bar{x}_1).\bar{n}_1 \geq 0 \tag{3}$$

The non-penetration condition ($g_N \geq 0$) prevents overlap between two bodies. When $g_N = 0$, contact occurs, and the normal stress indicates the contact force or pressure. Analyzing contact forces and pressure distribution involves satisfying the non-penetration condition and examining the stress vector components. Contact occurs when $g_N = 0$, with the reaction force (R_n) acting opposite to the surface's

normal vector. If the gap (g) is greater than zero, the surfaces are not in contact, and the reaction force is zero (Kuhn-Tucker condition [31]). See Eq. 4.

$$\begin{aligned} R_n &\leq 0 \\ g.R_n &= 0 \end{aligned} \tag{4}$$

To derive the normal-to-surface contact formulation for non-penetration, the strong form of the equilibrium equation can be expressed as Eq. 5.

$$\nabla.\sigma = b \qquad in \qquad \Omega \tag{5}$$

Here, σ is the stress tensor, ∇ is the gradient, b represents body forces, and Ω denotes the body domain. The normal component of the stress vector at the contact interface must be non-zero. Dirichlet (Γ_D) and Neumann (Γ_N) boundaries (with $\partial\Omega = \Gamma_N \cup \Gamma_D$) for Eq. 5 are defined in Eq. 6.

$$\begin{aligned} u &= u_g \qquad on \qquad \Gamma_D \\ \sigma.n &= t = t_g \qquad on \qquad \Gamma_N \end{aligned} \tag{6}$$

Here, u denotes displacement, u_g is the prescribed displacement, n is the boundary surface normal vector, and t represents the traction or stress vector with tg being its prescribed value. The weak form of the equilibrium equation is expressed in Eq. 7, where C_c is the penalty contact parameter indicating the contact contribution.

$$\int_{\Omega} \sigma : (\delta u \otimes \nabla)\, d\Omega - \int_{\Omega} (b.\delta u)\, d\Omega - \int_{\Gamma} (t.\ \delta u)\, d\Gamma + C_c \tag{7}$$

If ε denotes the penalty stiffness, the potential energy for the contact zone (Π_c) is given by Eq. 8.

$$\Pi_c = \frac{1}{2} \int_{\Gamma_c} \varepsilon.\ g^2 d\Gamma \tag{8}$$

Equation 8 applies only to contact problems without frictional sliding. Friction introduces dissipation, making the solution path-dependent. The weak form can be derived as Eq. 9 using Eqs. 7 and 8.

$$\int_{\Omega} \sigma : (\delta u \otimes \nabla)\, d\Omega - \int_{\Omega} (b.\delta u)\, d\Omega - \int_{\Gamma} (t.\ \delta u)\, d\Gamma - \int_{\Gamma_c} \varepsilon.\ g d\Gamma \tag{9}$$

2.2.2 Tangential contact

In the context of mechanical contact in the tangential direction, we encounter two scenarios: $sticking$ and $sliding$. When there is no sliding or relative motion (stick condition), a geometric constraint equation ensures that equal tangential displacements occur at the contact interface, preventing tangential movement. Conversely, constitutive law describes the frictional forces involved in frictional sliding, considering the normal force, relative tangential velocity, and slip distance.

The specific form of the constitutive law, which is essential for accurately depicting the behavior of contacting bodies, is determined by the characteristics of the contact interface and the materials involved. The stick condition, where both the relative tangential displacement and velocity become zero, is fundamental to a truly accurate representation of contact behavior.

Further exploration into stick, slip, and Coulomb friction contributes to a better comprehension of contact behavior. The stick condition corresponds to the scenario where both relative tangential displacement (g_T) and relative tangential velocity ($\dot{g}_T$) are zero, as illustrated in Eq. 10.

$$g_T = 0 \leftrightarrow \dot{g}_T = 0 \tag{10}$$

Enforcing the constraint condition of Eq. 10. It requires implementing appropriate constitutive relations for the tangential contact behavior during stick/slip motion. A penalty term (ε_T), is in rporated into Eq. 8, resulting in Eq. 11.

$$\Pi_c^P = \frac{1}{2} \int_{\Gamma_C} \left(\varepsilon_N (\bar{g}_N)^2 + \varepsilon_T\, g_T\, .\, g_T \right) dA, \qquad \varepsilon_N, \varepsilon_T\ > 0 \tag{11}$$

For pure stick at the contact interface, the variation of Eq. 11 is given by Eq. 12.

$$C_c^P = \int_{\Gamma_c} (\varepsilon_N \bar{g}_N \delta \bar{g}_N + \varepsilon_T g_T . \delta g_T) dA, \qquad \varepsilon_N, \varepsilon_T > 0 \tag{12}$$

Here, ε_N and ε_T are the penalty parameters. The penalty term Πc^P is added only for active constraints, defined by the penetration function g_N, and must be formulated for both normal and tangential contacts, with the latter applicable in the case of stick behavior. Eq. 13 addresses the slip condition.

$$C_c^{slip} = \int_{\Gamma_c} (\varepsilon_N \bar{g}_N \delta \bar{g}_N + t_T . \delta \bar{g}_T) dA, \qquad \varepsilon_N > 0 \tag{13}$$

In frictional sliding, a tangential stress vector (t_T) is determined by a friction constitutive law, such as the Coulomb friction.

2.2.3 Coulomb friction model

The Coulomb friction law, the most common constitutive equation, governs relative motion between contacting surfaces [25]. It states that relative motion occurs only when the frictional shear stress (τ) exceeds a critical threshold, as described by Coulomb's law (see Eq. 14).

$$\tau_T = -\mu \left| p_N \frac{\dot{g}_T}{\|\dot{g}_T\|} \right| \text{ if } \|\tau_T\| \geq \mu |P_N| \tag{14}$$

Here, μ is the sliding coefficient of friction, p_N is the normal pressure, and $\dot{g}T$ is the sliding velocity. Although μ is typically constant in the classical Coulomb law, it can vary due to surface roughness, sliding velocity, pressure, and temperature. Thus, the variable friction coefficient, denoted as $\mu = \mu(\dot{g}T, p_N, \theta)$, can be expressed as Eq. 15.

$$\mu(\dot{g}_T) = \mu_D + (\mu_S - \mu_D) e^{-d_C \|\dot{g}_T\|} \tag{15}$$

The static coefficient of friction, μ_S, indicates friction at zero relative sliding velocity, while μ_D represents the value at an intermediate sliding velocity. The decay coefficient d_c dictates how friction decreases with increasing relative velocity.

2.2.4 Elastic slip

Incremental slip due to elastic displacements from surface roughness is significant, even when the friction model indicates a stick phase [32]. This process results in slight displacements between contacting surfaces during the stick phase. To address this, the traditional Coulomb friction model is modified [25], transitioning from its conventional form (Fig.3 -(a)) to an adapted form (Fig.3 -(b)).
In $ABAQUS$, elastic slip can be characterized in two ways: by a fixed displacement magnitude or as a percentage relative to the characteristic element size of the surface. These options provide flexibility in accurately modelling elastic slips within the computational framework.

2.3 Implementation of Logarithmic Sine Sweep Loading

Sine sweep loading is a dynamic testing technique for evaluating the response structures or components across various frequencies. The frequency gradually increases or decreases over the specified range, known as the sweep rate. Linear or logarithmic sweep rates can be used [33]. Sine sweep testing allows for exploring dynamic behavior such as resonant frequencies, mode shapes, and damping characteristics. It is commonly used for modal analysis, reliability analysis, and fatigue testing. The input signal in this research is a sine wave with a logarithmic sweep rate determined by an equation involving the starting sweep frequency, sweep rate, and time [34]. The frequency increment is calculated using Eq. 16, where f_i represents the initial sweep frequency in Hz, R denotes the sweep rate in octave terms, and t corresponds to the time.

$$frequency(t) = \frac{f_i\left(-1+2^{Rt}\right)}{R\ln(2)} \tag{16}$$

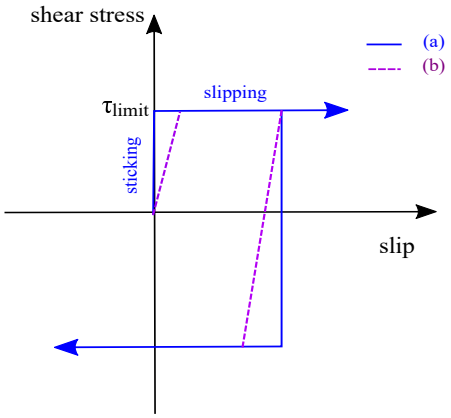

Fig. 3 – ideal (a) and penalty (b) stick-slip behavior

The value of R is obtained by dividing the total number of octaves ($N_{octaves}$) by the duration of the sweep. The calculation of the number of octaves, $N_{octaves}$, is based on Equation 17, where fo represents the final frequency of the sweep range.

$$N_{octaves} = \frac{\ln\left(\frac{f_o}{f_i}\right)}{\ln(2)} \tag{17}$$

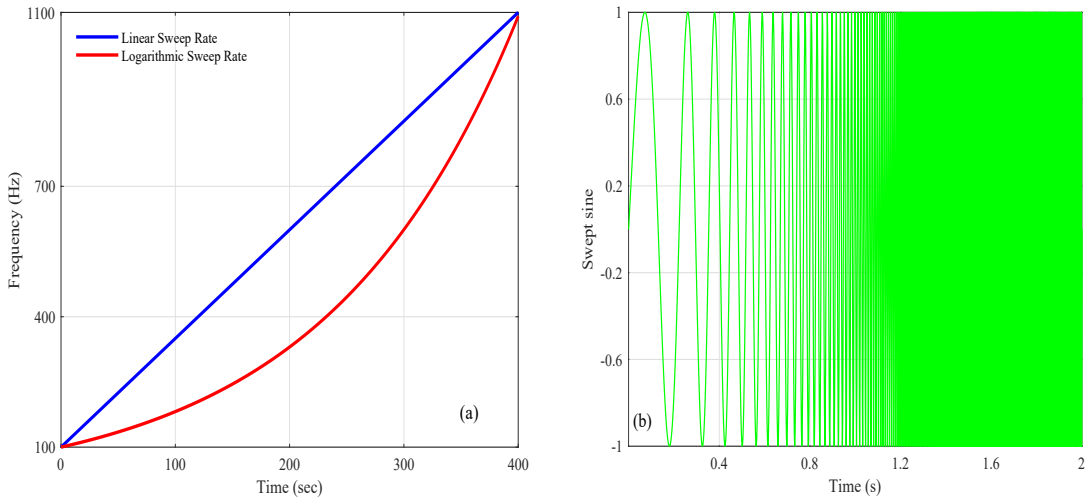

Figure 4 – (a) linear sweep rate vs. logarithmic sweep rate (b) time-sweep signal

2.4 Algorithm for Time and Frequency Domain Solutions

2.4.1 Frequency Domain Analysis

Frequency domain analysis is conducted using the Fast Fourier Transform (FFT) algorithm to analyze time-domain data and extract meaningful information in the frequency domain. The flowchart in Figure 5 outlines the steps for the procedure. The primary goal is to estimate the Frequency Response Function (FRF), which characterizes the system's response to external excitations.

2.4.2 Data Processing

We gather time-domain data from FE measurements, encompassing force and displacement signals. To minimize spectral leakage, a window function such as Hamming, Hanning, or Blackman is applied to the raw data [36].

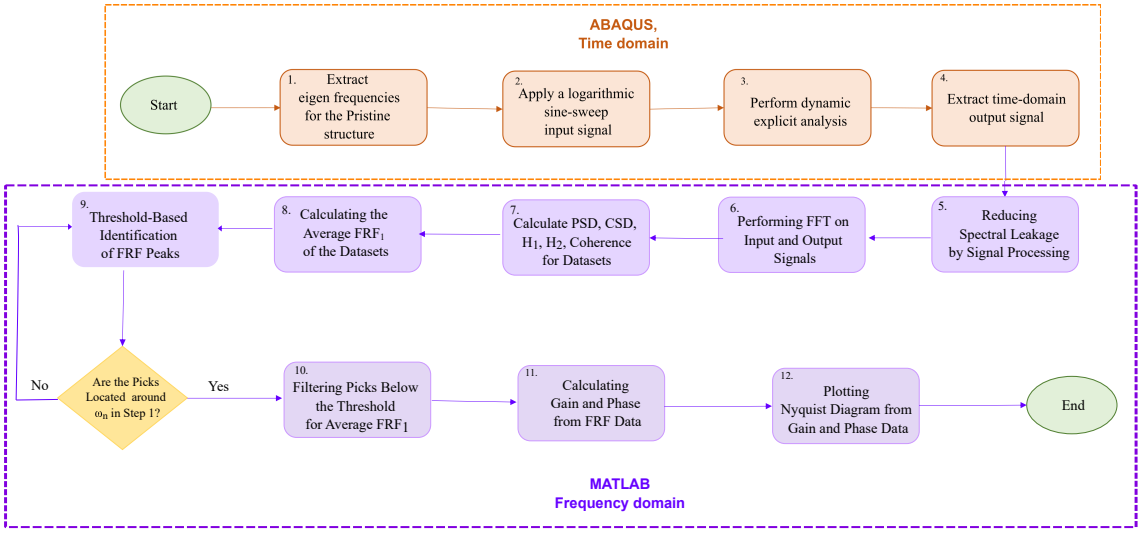

Fig. 5 – Time domain and frequency domain analysis steps [35]

2.4.3 Fast Fourier Transform

This study utilizes the FFT algorithm to efficiently convert the time-domain signal into the frequency domain [38]. By analyzing the coefficients of the Discrete Fourier Transform (DFT), the researchers obtain complex amplitudes that correspond to various frequency components.

2.4.4 Frequency Spectrum Analysis

Frequency spectrum analysis is a method used to examine the distribution of dominant frequencies and their magnitudes, providing valuable perspective into resonant frequencies and significant vibration modes within a system.

Power Spectral Density (PSD) is used to evaluate the energy distribution across different frequencies. It quantifies the power of a signal in the frequency domain. In this study, PSD is computed using FFT algorithm applied to the measured data [39].

$$PSD_{XX} = \frac{\mathrm{FFT(X)} \cdot \mathrm{FFT(X)}^{conj}}{f_{sampling} \cdot N_{sampling}} \tag{18}$$

Cross-spectral density (CSD) measures the cross-correlation between input and output signals in the frequency domain. It helps understand a system's behavior and identify transfer functions that describe the relationship between the two signals [40].

$$CSD_{XF} = \frac{\mathrm{FFT(X)} \cdot \mathrm{FFT(F)}^{conj}}{f_{sampling} \cdot N_{sampling}} \tag{19}$$

FRF estimation involves assessing the connection between input and output signals in the frequency domain. FRF_1 characterizes the transfer function from the input signal to the output signal and it is particularly informative in the anti-resonance region. FRF_2, on the other hand, is more informative in the resonance region, indicating the system's resistance to external forces. Coherence ($Coh.$), a measure of the linear association between input and output signals, is determined as the quotient of FRF_1 and FRF_1. This measure reveals the system's behavior. If its value is one or near one, the data is accurately measured [40].

$$\begin{aligned} FRF_1 &= \frac{\mathrm{CSD}_{XF}}{\mathrm{PSD}_{FF}} \\ FRF_2 &= \frac{\mathrm{PSD}_{XX}}{\mathrm{CSD}_{XF}} \\ Coh. &= \frac{|CSD_{XF}|^2}{|PSD_{XX}| * |PSD_{FF}|} \end{aligned} \tag{20}$$

Downsampling accommodates the discrepancy between the time step requirements for dynamic explicit convergence analysis and the conversion to the frequency domain. By reducing the data sets

obtained from dynamic explicit analysis, FRF_1 and FRF_2 are calculated for each down-sampled set. The average FRF across all sets is computed to reduce noise and inconsistencies from transforming time-domain data to the frequency domain.

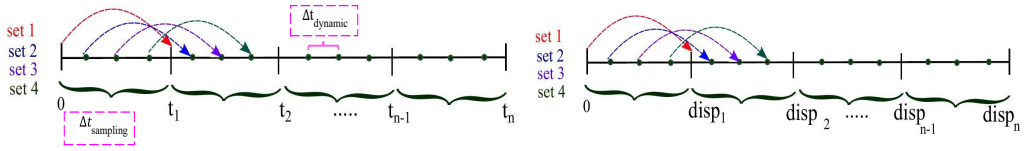

Fig. 6 – downsampling of data sets for computation of average FRF [35]

3. Results

3.1 Reliability Assessment of FE-Based Simulation

Mode shapes and natural frequencies of bending and torsional modes for the structure in Fig. 1 are shown in Fig. 7. Point-FRF of the pristine structure is presented in Fig. 8-(a) for a frequency range of 0 to 2000 Hz. The resonance frequencies align closely with the natural frequencies from Fig. 7, validating the algorithm outlined in Fig. 5. Figure 8-(b) reveals nested circles in the Nyquist plot, indicating the presence of multiple poles or resonant frequencies within the system, as depicted in Fig. 8-(a). It is important to highlight that the Nyquist plot of the undamped pristine structure exhibits perfect circularity due to the absence of factors causing deviations from this circular pattern.

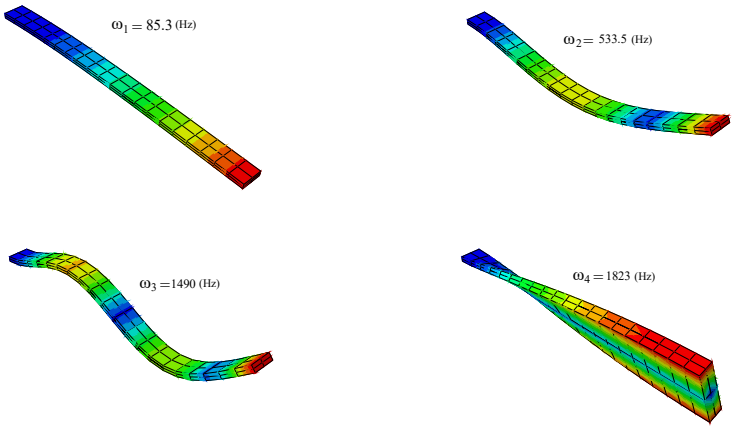

Fig. 7 – The mode shapes and the natural frequencies of the first three bending modes and the first torsion mode of the pristine structure

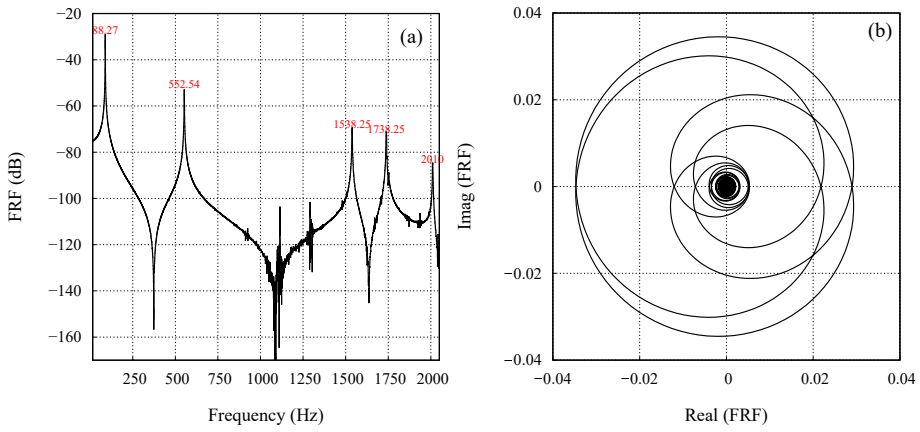

Fig. 8 – The point-FRF (a) and the Nyquist plot (b) of the pristine structure obtained using the algorithm of Fig. 5

3.2 Coefficient of friction sensitivity

This section aims to determine the optimal coefficient of friction COF value. The beam in Fig. 1, with two layers of thicknesses $t/4$ and $3t/4$, is analyzed. A 20% delamination is present longitudinally (Fig. 9-(a)) and transversely (Fig. 9-(b)) at the interface. COF ranges are based on sources like [39]. A two-second dynamic explicit analysis was conducted with the specified boundary conditions and loading.

Figure 10 shows that an optimal COF of 1.1 is for both longitudinal and transverse interface debonding, with more pronounced differences in transverse delamination.

Further analysis focuses on the impact of frictional contact between delaminated surfaces on the

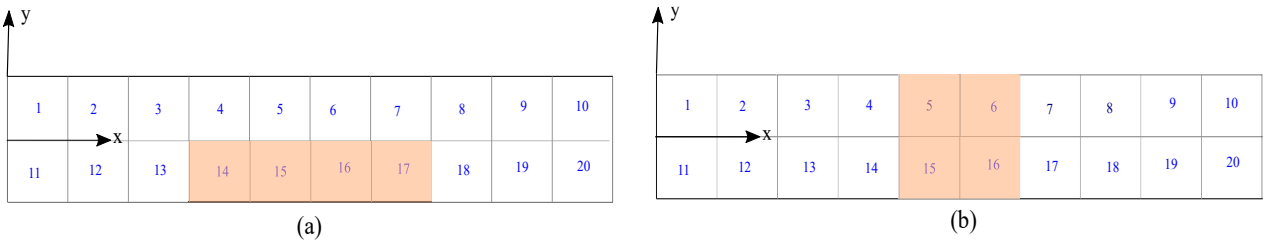

Fig. 9 – Visualization of delamination in 20 % of the layers interface, (a) along the length and (b) along the width, highlighted in color

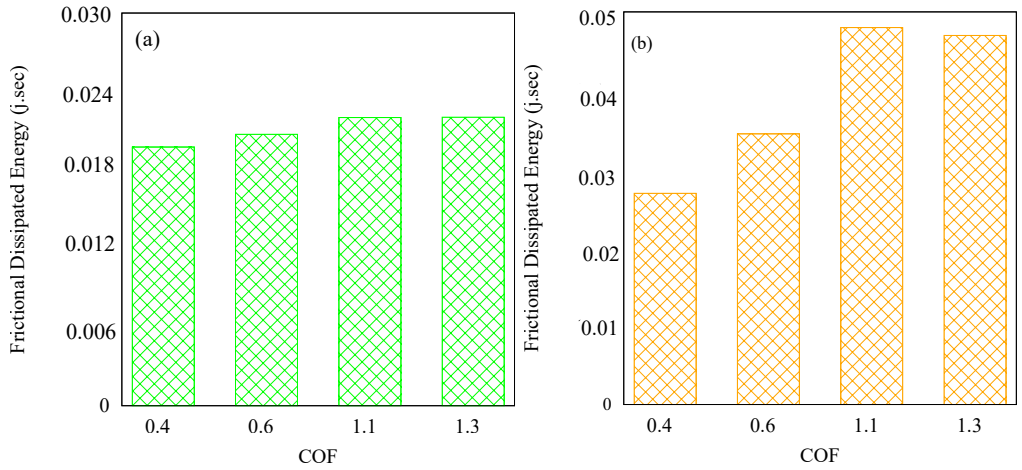

Fig. 10 – Frictional dissipated energy in the entire structure for (a) 20% delamination along the length of the interface (Fig. 9-(a)) and (b) 20% delamination along the width of the interface (Fig. 9-(b)) for various COFs.

structure's dynamic behavior. Parametric studies with COF set to 1.1 examined the influence comprehensively in both the time and frequency domains.

Figure 11-(a) shows the initial transient response diminishing over time, indicating system stabilization. Figure 11-(b) displays a sharp amplitude increase, suggesting that loading frequencies are near the beam's first natural frequency, resulting in resonance. Transverse delamination shows slightly higher peaks. In Fig.11-(c), the beam reaches a steady-state vibration pattern with similar periodic responses for both types of delamination. Figure11-(d) presents higher-order mode interactions, causing uneven response peaks and indicating complex vibration patterns due to the excitation frequencies aligning with multiple natural frequencies. The temporal history illustrates the transient response, resonance effects, steady-state behavior, and complex higher-order mode interactions in the beam with transverse and longitudinal delamination.

Phase maps of the structures for the loading node are depicted in Fig. 12, providing a graphical representation of the trajectories of the dynamical system in the phase plane. The phase portrait in Fig. 12 forms an elliptical shape, indicating periodic, harmonic motion. The data points for longitudinal delamination are more dispersed, covering a broader area, while those for transverse delamination are more concentrated, showing higher peak velocities and displacements. The dense clustering near the center reflects the stick phase with lower velocities and displacements. In contrast, the extended parts of the ellipse indicate the slip phase with higher velocities and displacements. The broader spread of data points in transverse delamination suggests greater energy dissipation through

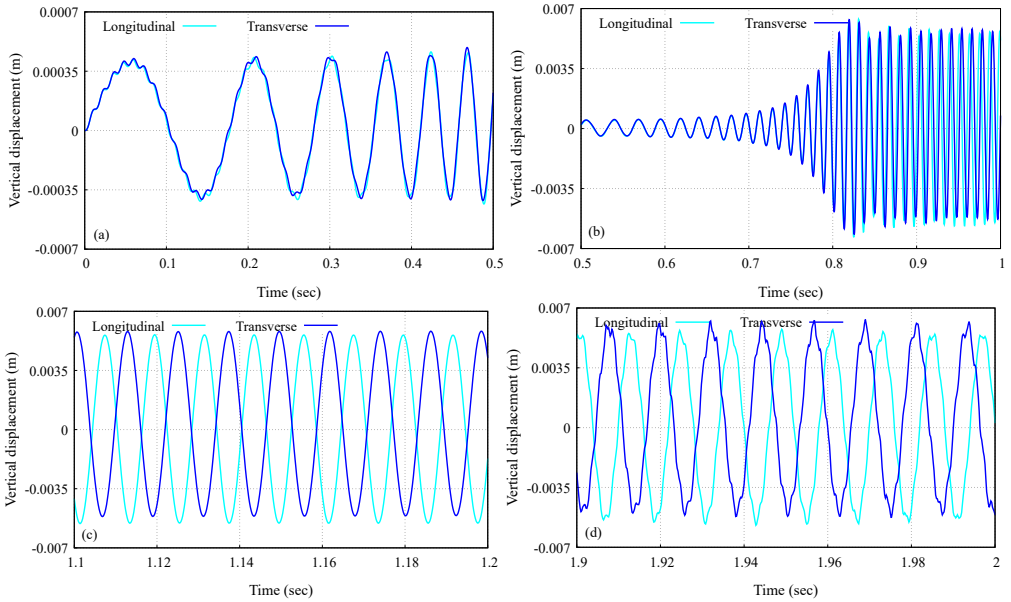

Fig. 11 – Temporal history of the structure with 20% longitudinal (Fig. 9-(a)) and transverse (Fig. 9-(b)) delamination

friction, aligning with prior findings of higher frictional energy dissipation in transverse debonding. The elliptical shape also implies that the applied logarithmic sine-sweep load induces a sinusoidal response, with distinct cycles indicating the structure's response to multiple harmonic frequencies.

Figure 13 illustrates the frictional dissipated energy in the structure during the analysis. In Fig.13-

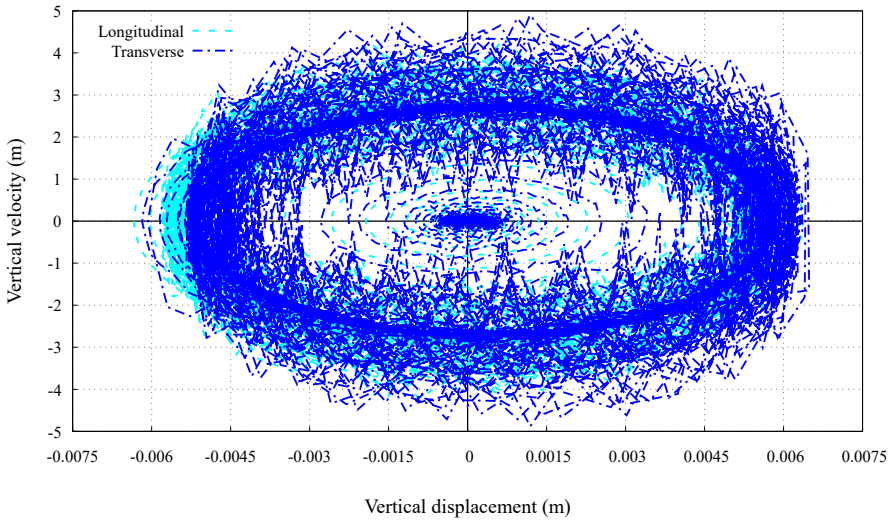

Fig. 12 – Phase portrait of the structure with 20% longitudinal (Fig. 9-(a)) and transverse (Fig. 9-(b)) delamination

(a), the initial moments of energy dissipation are highlighted, showing no dissipation during the stick phase between the delaminated interfaces. The curve's breaking point marks the transition from stick to slip. Fig.13-(b) reveals that, over time, the energy dissipation continues to increase steadily. Transverse delamination shows a more significant increase in energy dissipation, indicating a higher frictional interaction than longitudinal delamination for equal debonding percentages. This effect suggests that transverse delamination causes more interfacial sliding and energy loss due to friction compared to longitudinal delamination under the same loading conditions.

Figure 14-(a) quantifies the relations shown in Fig. 13. Figure 14-(a) shows that frictional energy dissipation in transverse delamination is more than twice that of longitudinal delamination, as observed in Fig.13. Figure14-(b) presents the strain energy ratio between damaged and pristine structures. Higher normalized strain energy for the structure with transverse damage implies that it is deforming more and thus storing more energy compared to the undamaged state. This effect indicates that

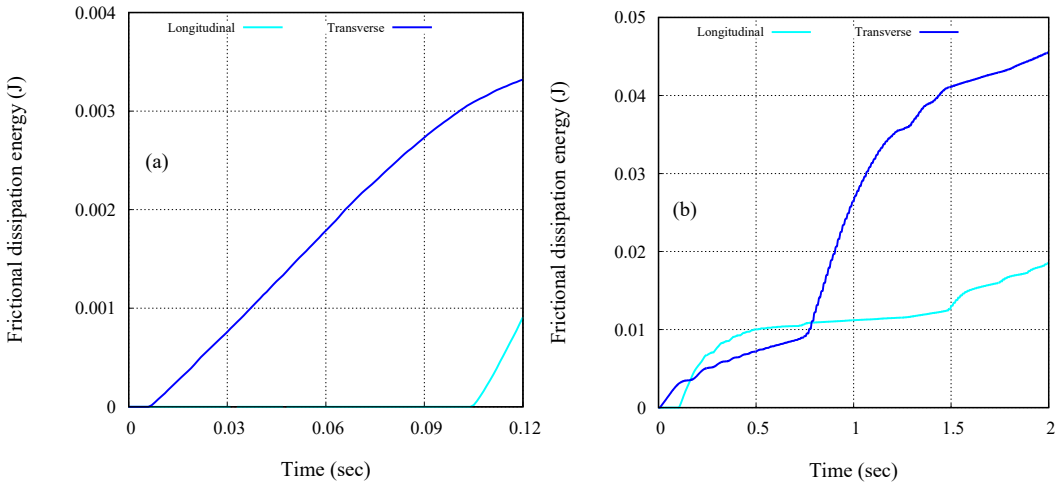

Fig. 13 – Temporal frictional dissipated energy in the entire structure for 20% longitudinal (Fig. 9-(a)) and transverse (Fig. 9-(b)) delamination

transverse delamination leads to a more severe impact on the structural integrity, causing both increased energy loss due to friction and greater deformation, resulting in higher stored strain energy.

Figure 15-(a) shows the FRF for structures with 20% transverse and longitudinal delamination. The

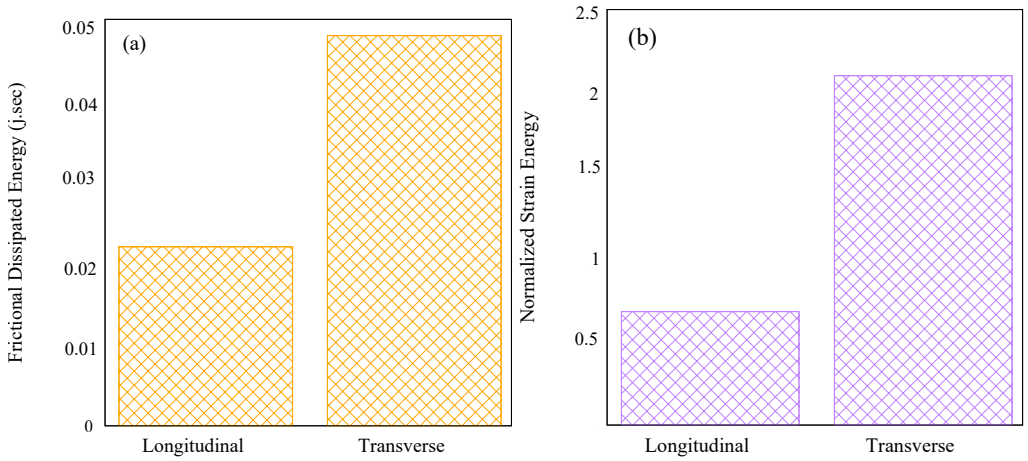

Fig. 14 – (a) Comparison of the amount of frictional dissipated energy in the entire structure (b) Normalized strain energy

resonance frequencies of the first two bending modes remain roughly unaffected, but a significant frequency shift is observed in the fourth resonance corresponding to the first torsional mode. The location of damage influences the frequency shift, with transverse damage exhibiting a more notable frequency reduction than longitudinal damage. The FRF peaks represent the system's natural frequencies, with the first three peaks corresponding to the bending modes and the fourth peak to the torsional mode. The longitudinal delamination and transverse delamination exhibit distinct resonance peaks. Still, the transverse delamination shows slightly higher resonance amplitudes, indicating a more significant vibration response and potentially higher energy dissipation.

The Nyquist plots in Fig. 15-(b) display non-circular patterns, indicating complex responses attributed to frictional contact properties at the delaminated interfaces. These patterns suggest additional coupling and non-linear behavior in the system. Larger loops in the Nyquist plot for transverse delamination signify greater nonlinearity and energy dissipation than longitudinal delamination. This difference aligns with the higher energy dissipation observed in the transverse delamination due to frictional effects at the interface.

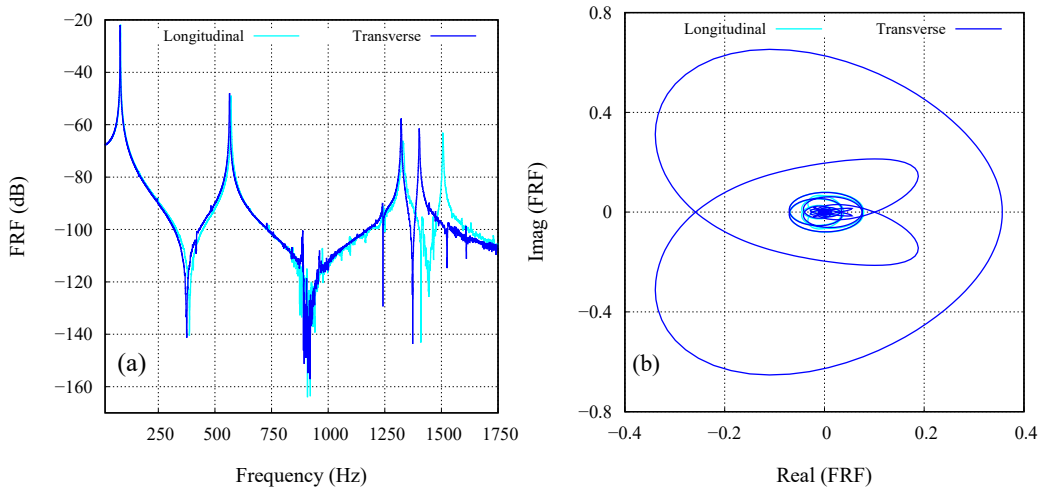

Fig. 15 – The point-FRF (a) and the Nyquist plot (b) of the structure with 20% longitudinal (Fig. 9-(a))) and transverse (Fig. 9-(b))) delamination

4. Conclusion

This study used a novel time and frequency domain approach to characterize frictional contact damping in delaminated structures. We evaluated whether frictional dissipated and strain energies are reliable parameters for tracing delamination. We concluded that these energies, along with the energy factor and the damped natural frequencies, are effective indicators for identifying delamination patterns. At equal percentages of delamination, different patterns (longitudinal and transverse) exhibited different behaviors. Delaminated cases showed significant variations in these values compared to the pristine state. These findings provide valuable information for developing advanced structural health monitoring tools, aiding in the design of more resilient engineering systems.

5. Contact Author Email Address

Email: shabnam.kiasat@polito.it (Sh. Kiasat).

6. Copyright Statement

References

[1] Adam T J, Liao G, Petersen J, Geier S, Finke B, Wierach P, Kwade A and Wiedemann M. Multifunctional composites for future energy storage in aerospace structures. *Energies*, Vol. 11, No. 2, pp 335, 2018.

[2] Chen Y, Zhang J, Li Z, Zhang H, Chen J, Yang W, Yu T, Liu W and Li Y. Manufacturing technology of lightweight fiber-reinforced composite structures in aerospace: current situation and toward intellectualization. *Aerospace*, Vol. 10, No. 3, p. 206, 2023.

[3] Saccone G, Favaloro N, Santoni F, Delfini A, Pastore R, Piergentili F, Albano M and Marchetti M. Concept Design for Manufacturing of New Advanced C/C Composites for Aerospace Applications. *Aerotecnica Missili & Spazio*, Vol. 101, No. 4, pp. 387-397, 2022.

[4] Patel M, Pardhi B, Chopara S and Pal M. Lightweight composite materials for automotive - a review. *Carbon*, Vol. 1, No. 2500, p. 151, 2018.

[5] Brøndsted P, Lilholt H and Lystrup A. Composite materials for wind power turbine blades. *Annual Review of Materials Research*, Vol. 35, pp 505-538, 2005.

[6] Ida N, Meyendorf N. Handbook of advanced nondestructive evaluation. *Springer International Publishing*, Cham, Switzerland, 2019.

[7] Alaimo A, Barracco A, Milazzo A, Orlando C. Structural Health Monitoring procedure for composite structures through the use of Artificial Neural Networks. *Aerotecnica Missili & Spazio*, Vol. 94, pp. 14-22, 2015.

[8] Montalvao D, Maia N M M and Ribeiro A. A review of vibration-based structural health monitoring with special emphasis on composite materials. *Shock and Vibration Digest*, Vol. 38, No. 4, pp 295-324, 2006.

[9] Kiasat Sh, Nobari A S, Filippi M, Carrera E. Characterization of viscoelastic damping mechanism in a delaminated structure. *Mechanical Systems and Signal Processing*, Vol. 219, pp 111600, 2024.

[10] Allix O and Ladevèze P. Interlaminar interface modelling for the prediction of delamination. *Composite Structures*, Vol. 22, pp 235-242, 1992.

[11] Camanho, P , Davila, C G and De Moura M F. Numerical simulation of mixed mode progressive delamination in composite materials. *Journal of Composite Materials*, Vol. 37, No. 16, pp 1415-1438, 2003.

[12] Pakdel H and Mohammadi B. Stiffness degradation of composite laminates due to matrix cracking and induced delamination during tension-tension fatigue. *Engineering Fracture Mechanics*, Vol. 216, No., pp., 2019.

[13] Salawu O S. Detection of structural damage through changes in frequency: a review. *Engineering Structures*, Vol. 19, No. 9, pp. 718-723, 1997.

[14] Paolozzi A, Peroni I. Identification of models of a composite plate for the purpose of damage detection. *AEROTEC. MISSILI SPAZIO*, Vol. 6, No. 7, pp. 119-129, 1988.

[15] Sharma D, Gupta S S and Batra R C. Mode localization in composite laminates. *Composite Structures*, Vol. 94, No. 8, pp. 2620-2631, 2012.

[16] Khazaee M, Nobari A S and Aliabadi M H F. Experimental investigation of delamination effects on modal damping of a CFRP laminate, using a statistical rationalization approach. In *Vibration-Based Techniques for Damage Detection and Localization in Engineering Structures*, 1st edition, World Scientific, 2018.

[17] Colombo Ch, Bhujangrao T, Libonati F and Vergani L. Effect of delamination on the fatigue life of GFRP: A thermographic and numerical study. *Composite Structures*, Vol. 218, pp. 152-161, 2019.

[18] Dahl P R. Solid friction damping of mechanical vibrations. *AIAA Journal*, Vol. 14, No. 12, pp 1675-1682, 1967.

[19] Griffin J H. A review of friction damping of turbine blade vibration. *International Journal of Turbo and Jet Engines*, Vol. 7, No. 3-4, pp 297-308, 1990.

[20] Gagnon L, Morandini M and Ghiringhelli G L. A review of friction damping modeling and testing. *Archive of Applied Mechanics*, Vol. 90, pp 107-126, 2020.

[21] Popp K, Panning L and Sextro W. Vibration damping by friction forces: theory and applications. *Journal of Vibration and Control*, Vol. 9, No. 3-4, pp 419-448, 2003.

[22] Park Y. M. and Kim K. J. Semi-active vibration control of space truss structures by friction damper for maximization of modal damping ratio. *Journal of Sound and Vibration*, Vol. 332, No. 20, pp 4817-4828, 2013.

[23] Zang M, Gao W and Lei Zh. A contact algorithm for 3D discrete and finite element contact problems based on penalty function method. *Computational Mechanics*, Vol. 48, pp 541-550, 2011.

[24] Chouly F and Hild P. On convergence of the penalty method for unilateral contact problems. *Applied Numerical Mathematics*, Vol. 65, pp 27-40, 2013.

[25] Wriggers P and Laursen T A. *Computational Contact Mechanics*. 2nd edition, Springer, 2006.

[26] Carrera E, Cinefra M, Petrolo M, and Zappino E. *Finite element analysis of structures through unified*

formulation. John Wiley & Sons, 2014.

[27] Reddy J N.*An introduction to the finite element method*. Vol. 3, McGraw-Hill, New York.

[28] Kikuchi N and Oden J T. *Contact problems in elasticity: a study of variational inequalities and finite element methods*. SIAM, 1988.

[29] Simo J C and Laursen T. An augmented Lagrangian treatment of contact problems involving friction. *Computers and Structures*, Vol. 42, No. 1, pp. 97-116, 1992.

[30] Wriggers P and Miehe C. Contact constraints within coupled thermomechanical analysis—a finite element model. *Computer Methods in Applied Mechanics and Engineering*, Vol. 113, No. 3-4, pp. 301-309, 1994.

[31] Kuhn H W, Tucker A W. Nonlinear Programming. *Proceedings of the Second Berkeley Symposium on Mathematical Statistics and Probability*, University of California Press, pp. 481-492, 1951.

[32] Carlberg J and Toyib B. Finite Element Modelling of Interlaminar Slip in Stress-Laminated Timber Decks, Friction Interaction Modelling Using Abaqus. *Proc Chalmers University of Technology*, Elsevier, Vol. 42, No. 1, pp. 97-116, 2012.

[33] Sauther E. Sine sweep vibration testing for modal response primer. *VR University*, https://vru.vibrationresearch.com/lesson/sweep-range-and-sweep-rate/, 2013.

[34] Umesh A M, and Zhao J. Sine sweep vibration test in high frequency range. *Sentek Dynamics News*, https://www.sentekdynamics.com/sentek-dynamics-news/2021/9/21/sine-sweep-in-high-frequency-range, 2021.

[35] Kiasat Sh, Nobari A S, Filippi M, and Carrera E. Frictional Contact in Delaminated Structures: Investigating its Effect on Dynamic Behavior and Application in Damage Detection. *Submitted*, 2024.

[36] MathWorks. Basic spectral analysis. *MathWorks*, https://ch.mathworks.com/help/signal/ug/basic-spectral-analysis.html, accessed on Feb2024.

[37] MathWorks. Spectral analysis. *MathWorks*, https://ch.mathworks.com/help/signal/ug/spectral-analysis.html, accessed on Feb2024.

[38] Oppenheim A V. *Discrete-time signal processing*. 1st edition, Pearson Education India, 1999.

[39] Engineers Edge. *Coefficient of friction equation and table chart*. Website, accessed on May2024, 2024.

[40] Martinson G D. Cross-spectral analysis. *Quantitative Methods of Data Analysis for the Physical Sciences and Engineering*, Cambridge University Press.